J. Fluid Mech. (2007), *vol.* 577, *pp.* 1–23.
doi:10.1017/S0022112006004472 Printed in the United Kingdom

Acoustic near field of a transonic instability wave packet

STÉPHANE LE DIZÈS[1] AND CHRISTOPHE MILLET[2]

[1]Institut de Recherche sur les Phénomènes Hors Équilibre, CNRS, 49 rue F. Joliot-Curie, BP 146, F-13384 Marseille cedex 13, France

[2]Laboratoire de Géophysique, CEA, BP 12, 91680 Bruyères-le-Châtel, France

(Received 21 July 2005 and in revised form 16 October 2006)

We consider the problem of acoustic radiation generated by a spatial instability wave on a weakly developing shear flow. Assuming a local WKBJ approximation for the instability wave near its maximum, we compute the acoustic pressure field by using a Fourier transform along the streamwise direction. When the instability wave is close to transonic near its maximum amplitude, approximations for this pressure field are obtained by a steepest descent method. A branch cut and several saddle points are shown possibly to contribute to the approximation. A detailed analysis of these contributions is provided. The modifications of the acoustic field when we pass from subsonic to supersonic are examined. In particular, the superdirective character of the acoustic field of subsonic instability waves and the directivity pattern of supersonic waves are shown to be both compatible with our mathematical description and associated with a single saddle-point contribution.

The acoustic near field is also shown to possess a caustic around which a specific approximation is derived. In a large region of the physical space, the near field is composed of two saddle-point contributions. Close to the shear flow, one of these contributions degenerates into a branch-point contribution which always becomes dominant over the instability wave downstream of a location that is computed. An interesting phenomenon is observed in certain regions downstream of the maximum: the transverse behaviour of the instability wave has to be exponentially growing far from the shear layer to match the acoustic field. We demonstrate that this phenomenon neither requires a branch-point contribution nor a supersonic instability wave.

1. Introduction

The processes by which sound is generated from fluid dynamics have been the subject of numerous works since Lighthill (1952). It was rapidly recognized that small-scale turbulence and coherent structures can both generate sound with different characteristics (Crighton 1975; Goldstein 1984). In terms of acoustics, turbulence is usually described as moving sources of quadrupoles, whereas coherent structures are often considered as oscillating surfaces, or wavy walls. In this analogy, the oscillating surface mimics a coherent structure in the form of an instability wave. The sound generated by such a surface is easily calculated as it amounts to solving the Helmholtz equation with simple boundary conditions on a plane. In a fluid at rest, it is found that there is generation of sound only if the phase velocity of the oscillating surface is larger than the ambient speed of sound a_0, that is, for supersonic convective Mach number $M_c \equiv \omega/(ka_0) > 1$. The sound is then a (Mach) wave propagating in the

angular direction defined by the Mach angle relation $\cos\theta = 1/M_c$. In this framework, the acoustic far field is considered as a superimposition of Mach waves generated by perturbations. In particular, the most intense noise radiation direction in the far field is expected to be given by the Mach angle obtained from the convective Mach number of the most amplified instability wave, that is, $M_c = \omega/(\alpha a_0)$, where α is the wavenumber at maximum amplitude.

In supersonic flows, several comparisons have been made between acoustic field and instability characteristics using this approach. Most of them concern supersonic jets. We can cite Yu & Dosanjh (1971), McLaughlin, Morrison & Troutt (1975, 1977), Morrison & McLaughlin (1980), Stromberg, McLaughlin & Troutt (1980) and Troutt & McLaughlin (1982) among the experimental works, and Tam, Chen & Seiner (1992), Mitchell, Lele & Moin (1997), Morris *et al.* (1997), Malik & Chang (2000) and Mohseni, Colonius & Freund (2002) among the numerical and theoretical works. For highly supersonic jets, it was shown that there is a good correlation between the properties of the most unstable (helical) mode and the acoustic far-field characteristics. For low supersonic jets ($M < 1.5$), it was, however, observed that the acoustic field is dominated by a less unstable axisymmetric mode, in agreement with the most unstable helical mode having a subsonic convective Mach number (see Millet & Casalis 2004). Tam (1995) demonstrated that nonlinear harmonics or the interaction of an instability wave with a shock cell structure of an imperfectly expanded supersonic jet are sources of noise which can also be described in the same framework.

The sound generated by coherent structures in subsonic jets or mixing layers has been understood using the same analogy. However, the sound is not directly created by the phase speed of the instability wave, but by its amplitude modulation whose wavenumber spectrum possesses supersonic phase velocities. To determine sound radiation, a global solution of the entire wave-propagation phenomenon is necessary. Crighton & Huerre (1990) analysed how the acoustic field depends on the amplitude modulation profile by seeking asymptotic expansions of the general integral solution. They suggested that the decay changes from exponential to algebraic around some penetration distance. They found a *superdirective* behaviour in the acoustic field when the penetration distance and the acoustic wavelength are comparable, a condition that can be met for a Gaussian amplitude modulation.

For a given instability wave packet, the acoustic far field is provided by the same expression for both supersonic and subsonic waves. This expression is easily obtained by the method of stationary phase and depends strongly on the large-scale envelope function that modulates the instability wave. For a Gaussian wave packet, the two-dimensional pressure far field has the following form (e.g. Avital & Sandham 1997)

$$\langle p^2(r,\theta)\rangle \sim \frac{(\sin\theta)^2}{r}\exp[-\delta(1-M_c\cos\theta)^2], \tag{1.1}$$

where δ is a constant which is proportional to the integral scale of the wave packet. For small convective Mach numbers, the acoustic far field is exponentially small in all directions and maximum in the downstream direction for which $\cos\theta$ is of order unity. The antenna factor (exponential term in (1.1)) has been observed in measurements by Laufer & Yen (1983) on a low-Mach-number jet, and a theoretical model based on global modes has been provided by Cooper & Crighton (2000). Colonius, Lele & Moin (1997) and Freund (2001), among others, were also able to capture the superdirective behaviour associated with the antenna factor in numerical simulations of mixing layer and jet, respectively. Expression (1.1) demonstrates that, for large Mach numbers, the acoustic far field is dominant in the Mach angle direction. However, as in the subsonic

case, it is also exponentially small in the downstream direction. It is worth mentioning that it is only for transonic convective Mach numbers ($M_c \sim 1$) that the acoustic field is not exponentially small for small angles. We shall see below that it is for this reason that, in the transonic regime, the interaction of the instability wave with the acoustic field can be captured by a local analysis.

The link between the instability wave and the acoustic field was first examined in the context of shear flows by Tam & Morris (1980). They computed the acoustic far field using the local stability characteristics of spatial developing subsonic instability waves. In the present paper, we shall use some of their data to illustrate our calculation of the near field. In particular, we shall analyse how the pressure directivity varies in the near field.

For supersonic flows, Tam & Burton (1984*a*, *b*) pointed out the importance of the matching procedure between the instability wave and the acoustic field expression to provide the characteristics of the near field. They showed that as the spatial behaviour of a supersonic instability wave changes from growth to decay, the transverse structure of the wave is also radically modified. The instability wave is localized in the shear flow during its growth, but when it reaches its maximum and becomes damped, the transverse behaviour of the instability wave is no longer bounded. Tam & Burton showed that the matching with the acoustic field could impose the spatially damped instability wave to be exponentially increasing in the transverse direction. This peculiarity was associated by Tam & Burton with the crossing of the branch cut defined in the integral expression of the acoustic field by the local complex wavenumber of the instability wave. We shall see, in the present paper, that this phenomenon actually depends on other characteristics of the wave packets, and that it can also affect subsonic wave packets.

Tam & Burton (1984*a*, *b*), in their matching procedure, only considered the acoustic contribution of the instability wave. They did not consider the feedback of the acoustic field on the shear flow. For small θ, that is in the shear flow, the contribution given by (1.1) has to be compared with the instability wave. Both are exponentially small for non-transonic Mach numbers, but the acoustic contribution is always larger than the instability wave packet, sufficiently far downstream, as the acoustic field decreases algebraically. To understand how and where the instability wave is superseded by the acoustic field constitutes one of the main motivations of this work. In the transonic regime, the acoustic far field remains algebraic within the shear flow. It is therefore expected to become dominant over the instability wave packet that has generated it downstream of a location near the instability wave maximum. The transonic hypothesis will then permit us to describe the interplay between the instability wave and its acoustic field by a local analysis near the instability wave maximum.

The paper is organized as follows. In § 2, the wavy wall analogy framework is presented for two-dimensional flows. The scalings that we consider are introduced. The general integral expression for the acoustic pressure field is shown to reduce for our scalings to a simple generic problem which is treatable by asymptotic techniques. Asymptotic estimates for the integral are obtained through a steepest descent analysis in § 4. The different contributions (branch point, saddle points) are analysed in detail, in particular, to identify the regions where they are present. Stokes lines and anti-Stokes lines which characterize the approximation are in particular determined. The acoustic field is also shown to exhibit a caustic around which a specific approximation is obtained in that section. Features of the acoustic field are computed in § 4 for a few specific cases. In § 5, the form of the acoustic field close to the shear flow is studied. A branch-point contribution is shown to be present in the shear flow downstream

of a streamwise location which is computed. The condition of matching the acoustic field with the instability wave is also analysed. It is shown that it may require an exponential growth of the instability wave in the transverse direction. The last section briefly summarizes the main results of the article. An application of the results to the data provided by Tam & Morris (1980) for a two-dimensional mixing layer is also provided.

2. The basic equations

We consider a two-dimensional spatial instability wave of real frequency ω in a pre-existing two-dimensional mixing layer. The basic flow is assumed to be weakly non-parallel, such that the pressure of the instability wave can be described by a local plane wave approximation (WKBJ approximation)

$$p_i(x, y; X) = q_i(y; X) \exp\left\{\frac{\mathrm{i}}{\varepsilon}\int^X \alpha(s)\,\mathrm{d}s\right\}, \tag{2.1}$$

where the small parameter ε measures the non-parallel character of the flow along the streamwise direction x. This parameter can be defined, for instance, as the ratio of a characteristic instability wavelength by a streamwise evolution length. The non-parallel character implies that the streamwise velocity and density of the base flow depend on the transverse coordinate y and on a slow variable $X = \varepsilon x$. The local complex wavenumber $\alpha(X)$ varies on the same slow streamwise variable. It is obtained by solving a local Rayleigh equation for the transverse structure $q_i(y; X)$ of the perturbation pressure with suitable boundary conditions. We shall see below that boundary conditions are not a trivial matter. *A priori*, they should be deduced from the condition of matching with the acoustic field. We shall come back to this issue at the end of the paper. In the following, we assume that $\alpha(X)$ is known and that the matching can be performed.

If the fluid is at rest far from the shear flow, the instability wave pressure behaves for large y ($y > 0$) as a complex exponential

$$p_i(x, y; X) \sim p_i^{(\infty)}(x; \varepsilon) \exp\left\{-\sqrt{\alpha^2(X) - k_0^2}\; y\right\}, \tag{2.2}$$

where the branch point k_0 is defined from the speed of sound a_0 by $k_0 = \omega/a_0$, and

$$p_i^{(\infty)}(x; \varepsilon) = A(X) \exp\left\{\frac{\mathrm{i}}{\varepsilon}\int^X \alpha(s)\,\mathrm{d}s\right\}. \tag{2.3}$$

In the dimensionless wave equation of Crighton & Huerre (1990), the length scale is given by the wavelength $1/\alpha$, whereas Tam & Burton (1984*a*) used the initial thickness of the mixing layer. Using the dimensionless space coordinates of Tam & Burton (1984*a*), the role of the convective Mach number of Crighton & Huerre (1990) is played by k_0 in our problem.

As mentioned above, the definition of the square root results from a condition of matching. We shall see in § 6 that in certain conditions, the matching imposes $\mathrm{Re}(\sqrt{\alpha^2 - k_0^2}) < 0$ such that the instability wave is exponentially growing in the transverse direction, for $y > 0$.

In the outer region (far from the shear flow), the pressure field $p_0(x, y)$ satisfies the Helmholtz equation

$$\frac{\partial^2 p_0}{\partial x^2} + \frac{\partial^2 p_0}{\partial y^2} + k_0^2 p_0 = 0. \tag{2.4}$$

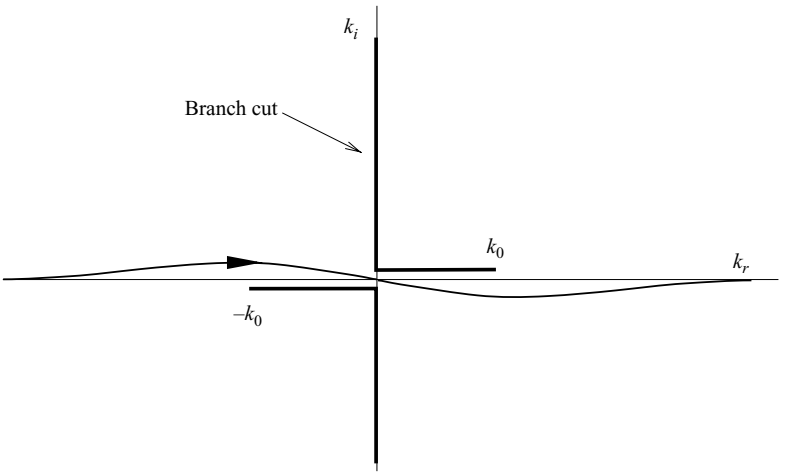

FIGURE 1. Integration contour and branch cut in the complex k-plane for the definition of the acoustic field expression (2.6).

Tam & Morris (1980) showed that a solution to (2.4) can be matched to (2.2) if we assume that it satisfies the boundary condition

$$p_0(x, 0) = p_i^{(\infty)}(x; \varepsilon). \tag{2.5}$$

This constitutes the oscillating surface, or wavy wall analogy. The general solution of this 'outer' problem, that we shall call the *acoustic field*, can be written

$$p_0(x, y; \varepsilon) = \int_{-\infty}^{+\infty} \hat{p}_i^{(\infty)}(k; \varepsilon)\, \exp(\mathrm{i}kx - \sqrt{k^2 - k_0^2}\, y)\, \mathrm{d}k, \tag{2.6}$$

where

$$\hat{p}_i^{(\infty)}(k; \varepsilon) = \frac{1}{2\pi} \int_{-\infty}^{+\infty} p_i^{(\infty)}(x; \varepsilon)\, \mathrm{e}^{-\mathrm{i}kx}\, \mathrm{d}x, \tag{2.7}$$

defines the Fourier transform $\hat{p}_i^{(\infty)}(k; \varepsilon)$ of $p_i^{(\infty)}(x; \varepsilon)$.

The branch cut is defined by the condition $-\pi/2 \leqslant \arg(\sqrt{k^2 - k_0^2}) < \pi/2$, such that the contributions to the integral as y tends to infinity are bounded or represent outgoing waves. This corresponds to a causality condition which guarantees that the integral tends to zero as $y \to \infty$ for any frequency with a positive imaginary part ($\mathrm{Im}(k_0) > 0$). The integration contour and the branch cut are illustrated in figure 1.

The behaviour of the acoustic field for large values of $x^2 + y^2$ is readily obtained from (2.6) by the steepest-descent method. If $x = r\cos\theta$ and $y = r\sin\theta$, we obtain as $r \to \infty$, the acoustic far-field expression

$$p(r, \theta) \sim \sqrt{\frac{2\pi k_0}{r}}\, \sin\theta\, \exp(\mathrm{i}k_0 r - \mathrm{i}\pi/4) \hat{p}_i^{(\infty)}(k_0 \cos\theta; \varepsilon). \tag{2.8}$$

Equation (1.1) is obtained from this expression with a Gaussian wave packet for $p_i^{(\infty)}$. Such a Gaussian wavepacket is generically obtained for $p_i^{(\infty)}$ from (2.3) in the neighbourhood of its maximum location X_m where $\mathrm{Im}(\alpha(X_m)) = 0$. Indeed, using k_0 to non-dimensionalize all spatial variables (this amounts to replacing k_0 by 1 in the formulae

given above), (2.3) reduces at leading order to

$$p_{im}^{(\infty)}(x;\varepsilon) \sim A_m \exp\left\{-\mathrm{e}^{-\mathrm{i}\chi}\frac{|\alpha_m'|(X-X_m)^2}{2\varepsilon}\right\}\mathrm{e}^{\mathrm{i}\alpha_m x}, \tag{2.9}$$

where $\alpha_m = \alpha(X_m)$, α_m' is the derivative of α with respect to X, evaluated at X_m and

$$\chi = \tfrac{1}{2}\pi - \arg(\alpha_m'). \tag{2.10}$$

Expression (2.9) is valid as long as higher-order terms, such as $\alpha_m''(X-X)^3/(3\varepsilon)$, do not intervene in the exponential. This requires that $|X-X_m| \ll \varepsilon^{1/3}$ or equivalently

$$|x-x_m| \ll \varepsilon^{-2/3}. \tag{2.11}$$

In the following, we also assume that the maximum is not degenerated, that is the angle χ is such that $-\pi/2 < \chi < \pi/2$. When $\chi = 0$, or equivalently α_m' is purely imaginary, expression (2.9) is just a wave of wavenumber α_m modulated by a Gaussian amplitude, as considered by Crighton & Huerre (1990).

Close to $k = \alpha_m$, we expect the Fourier transform of $p_i^{(\infty)}$ to be given by the Fourier transform of (2.9). Thus, to the lowest order, $\hat{p}_{im}^{(\infty)}$ can be written as

$$\hat{p}_{im}^{(\infty)}(k;\varepsilon) \sim \frac{A_m \mathrm{e}^{\mathrm{i}\chi/2}}{\sqrt{2\pi\bar{\varepsilon}}}\exp\left\{-\mathrm{e}^{\mathrm{i}\chi}\frac{(k-\alpha_m)^2}{2\bar{\varepsilon}}\right\}\mathrm{e}^{-\mathrm{i}(k-\alpha_m)x_m}, \tag{2.12}$$

with $\bar{\varepsilon} = \varepsilon|\alpha_m'|$. It will be convenient to write (2.12), using (2.9), as

$$\hat{p}_{im}^{(\infty)}(k;\varepsilon) \sim \frac{\mathrm{e}^{\mathrm{i}\chi/2}p_{im}^{(\infty)}(x;\varepsilon)}{\sqrt{2\pi\bar{\varepsilon}}}\exp\left\{-\mathrm{e}^{\mathrm{i}\chi}\frac{[k-\alpha_m-\alpha_m'(X-X_m)]^2}{2\bar{\varepsilon}}\right\}\mathrm{e}^{-\mathrm{i}kx}. \tag{2.13}$$

Our purpose is to analyse the way in which the instability wave is transformed into the acoustic far field (2.8). As explained in § 1, when instability wavenumber α_m and branch point k_0 are close to each other, this transformation is expected to occur in the neighbourhood of X_m. We shall characterize the size of this neighbourhood by a new small positive parameter μ. The scalings for the variables k and y in term of μ can be obtained from expressions (2.6) and (2.12). We immediately see that all the wavenumbers have to be in a $O(\mu)$ neighbourhood of the branch point. Moreover, the acoustic field component associated with the square root term in (2.6) is present at the same order if $y = O(\mu^{3/2}/\varepsilon)$. The corresponding physical domain is indicated in figure 2.

In the following, we shall assume that the small parameter μ satisfies the condition

$$\sqrt{\varepsilon} \ll \mu \ll \varepsilon^{1/3}. \tag{2.14}$$

The condition $\mu \ll \varepsilon^{1/3}$ guarantees that the Gaussian approximation for the wave packet can be used. The other condition $\mu \gg \sqrt{\varepsilon}$ is to guarantee that the integral (2.6) remains, in the domain of study, an integral with a rapidly varying phase, allowing the asymptotic analysis performed in the next section. Under hypothesis (2.14), the streamwise scale μ/ε of the acoustic field is larger than the wave-packet scale $1/\sqrt{\varepsilon}$, but smaller than the large evolution scale or integral scale $1/\varepsilon$ of the base flow. Note that the domain of study contains the small angle direction ($\tan\theta = O(\sqrt{\mu})$) along which the acoustic far field is maximum.

For the analysis, it is convenient to introduce the local variables $\bar{X}$, $\bar{Y}$ and $\bar{K}$ defined by

$$\bar{X} = \frac{X-X_m}{\mu} = \frac{\varepsilon(x-x_m)}{\mu}, \tag{2.15a}$$

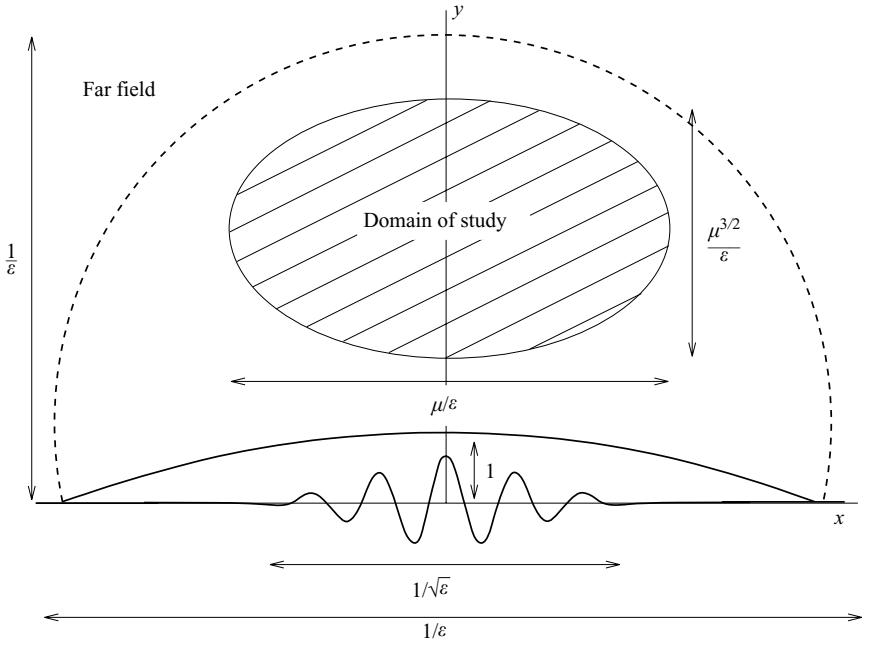

FIGURE 2. Location of the region of study in the acoustic field region (delimited from below by the solid curve). The far-field region is above the dashed curve. The wave-packet scale $1/\sqrt{\varepsilon}$ and the integral scale $1/\varepsilon$ are indicated on the plot of the instability wave amplitude. The parameter μ is such that $\sqrt{\varepsilon} \ll \mu \ll \varepsilon^{1/3}$.

$$\bar{Y} = \frac{\varepsilon y}{\mu^{3/2}}, \tag{2.15b}$$

$$\bar{K} = \frac{k-1}{\mu}. \tag{2.15c}$$

The local instability wavenumber α_m is also assumed to be in the $O(\mu)$ neighbourhood of the branch point $k_0 = 1$. The parameter μ can then be renormalized such that α_m can be written, up to $o(\mu)$ terms, as

$$\alpha(X_m) \sim 1 + \bar{\alpha}\mu, \tag{2.16}$$

where $\bar{\alpha} = 1$ for the (weakly) subsonic case and $\bar{\alpha} = -1$ for the (weakly) supersonic case. The transonic case ($\bar{\alpha} = 0$) corresponds to configurations where $|\alpha_m - 1| \ll \mu$.

Substituting the above expansions in (2.6) with (2.13), the acoustic pressure field can be written at leading order as

$$p_0(\bar{X}, \bar{Y}; \varepsilon, \mu) \sim q(x; \varepsilon, \mu) \int_{-\infty}^{+\infty} \exp\left\{ \frac{\mu^2 \psi(\bar{K}, \bar{X}, \bar{Y})}{\bar{\varepsilon}} \right\} \mathrm{d}\bar{K}, \tag{2.17}$$

with

$$q(x; \varepsilon, \mu) = \frac{\mu \mathrm{e}^{\mathrm{i}\chi/2}}{\sqrt{2\pi\bar{\varepsilon}}} p_{im}^{(\infty)}(x; \varepsilon), \tag{2.18a}$$

$$\psi(\bar{K}, \bar{X}, \bar{Y}) = -\tfrac{1}{2}\mathrm{e}^{\mathrm{i}\chi}(\bar{K} - \bar{\alpha} - \alpha'_m \bar{X})^2 - |\alpha'_m| \sqrt{2\bar{K}}\bar{Y}. \tag{2.18b}$$

We shall see in § 6 that this expression is convenient for analyzing the matching of the acoustic field with the instability wave. For an estimation of the integral in

a general framework, it is useful to go one step further in the reduction. For this purpose, we define renormalized variables

$$\hat{X} = |\alpha'_m|\bar{X}, \tag{2.19a}$$

$$\hat{Y} = \frac{|\alpha'_m|\bar{Y}}{|N(\hat{X})|^{3/2}}, \tag{2.19b}$$

$$\hat{K} = \frac{\bar{K}}{2N(\hat{X})}, \tag{2.19c}$$

$$\hat{\varepsilon} = \frac{\bar{\varepsilon}}{2[\mu N(\hat{X})]^2}, \tag{2.19d}$$

where the real function $N(\hat{X}) > 0$ is defined by

$$N(\hat{X})\mathrm{e}^{\mathrm{i}\phi(\hat{X})} = \hat{X} - \mathrm{i}\mathrm{e}^{\mathrm{i}\chi}\bar{\alpha}. \tag{2.20}$$

In contrast with χ, which is a constant parameter characterizing the instability wave near its maximum, the other parameters $\hat{Y}$ and ϕ are functions that vary with the location $\hat{X}$. For instance, as $\hat{X}$ varies from $-\infty$ to $+\infty$, the function ϕ varies from $-\pi$ to 0^- in the subsonic case ($\bar{\alpha} = 1$), and from $+\pi$ to 0^+ in the supersonic case ($\bar{\alpha} = -1$). In the transonic case, ϕ remains constant and equal to zero.

With these new variables, the expression for p_0 becomes

$$p_0(\hat{X}, \hat{Y}; \varepsilon, \mu) \sim \hat{q}(x; \varepsilon, \mu) \int_{-\infty}^{+\infty} \exp\left\{\frac{\hat{\psi}(\hat{K}, \hat{Y}, \phi, \chi)}{\hat{\varepsilon}}\right\} \mathrm{d}\hat{K}, \tag{2.21}$$

with

$$\hat{q}(x; \varepsilon, \mu) = \frac{\sqrt{2}\mu N(\hat{X})\mathrm{e}^{\mathrm{i}\chi/2}}{\sqrt{\pi\bar{\varepsilon}}} A_m \exp\left\{-\mathrm{e}^{\mathrm{i}\chi}\frac{\mu^2\bar{\alpha}^2}{2\bar{\varepsilon}}\right\} \mathrm{e}^{\mathrm{i}x + i\bar{\alpha}\mu x_m}, \tag{2.22a}$$

$$\hat{\psi}(\hat{K}, \hat{Y}, \phi, \chi) = -\sqrt{\hat{K}}\hat{Y} + \mathrm{i}\mathrm{e}^{\mathrm{i}\phi}\hat{K} - \mathrm{e}^{\mathrm{i}\chi}\hat{K}^2. \tag{2.22b}$$

In the complex $\hat{K}$-plane, there is now a unique branch cut, issuing from the branch point $\hat{K} = 0$. To be in agreement with the definition of the Fourier transform, this singularity must remain above the integration contour.

3. Steepest descent analysis

In this section, an asymptotic estimate of

$$I(\hat{Y}, \phi, \chi) = \int_{-\infty}^{+\infty} \exp\left\{\frac{\hat{\psi}(\hat{K}, \hat{Y}, \phi, \chi)}{\hat{\varepsilon}}\right\} \mathrm{d}\hat{K}, \tag{3.1}$$

is obtained as $\hat{\varepsilon} \to 0$. The form of this expression is well-adapted to the steepest-descent method as explained in several textbooks (e.g. Erdélyi 1956). The idea of the method is to use the analyticity of the integrand to justify deforming the integration contour, initially taken along the real axis, to a new contour on which the phase $\hat{\psi}$ has a constant imaginary part. Such a contour is called a constant-phase contour, or equivalently, a steepest-descent contour. The contributions to the integral are then found to come from saddle points and from singularities that cannot be avoided.

3.1. *Saddle-point contributions and integration contour*

The saddle points $\hat{K}_s$ are points in the complex $\hat{K}$-plane at which two or more distinct steepest-descent curves can intersect. They are defined by

$$\partial_{\hat{K}}\hat{\psi}(\hat{K}_s) = 0,$$

that is, substituting (2.22*b*) into the above equation, we obtain

$$-\frac{\hat{Y}}{2\sqrt{\hat{K}_s}} + \mathrm{i}\mathrm{e}^{\mathrm{i}\phi} - 2\mathrm{e}^{\mathrm{i}\chi}\hat{K}_s = 0. \tag{3.2}$$

Equation (3.2) possesses three complex solutions for $\sqrt{\hat{K}_s}$ which may be computed using Cartan's method. However, it provides at most only two different values of $\hat{K}_s$ for a given Riemann sheet, that is, for a given 2π range of variation of $\hat{K}$. We shall denote these saddle points by $\hat{K}_s^{(1)}$ and $\hat{K}_s^{(2)}$. The unique singularity that can also contribute to the integral is the branch point $\hat{K} = 0$. We shall see below that except for $\hat{Y} \to 0$, this singularity can always be avoided by deforming the branch cut issuing from $\hat{K} = 0$.

The leading-order contribution from a simple non-zero saddle point $\hat{K}_s^{(j)}$, where j is an index which will be defined in the following, is found to be

$$I_s^{(j)}(\hat{Y}, \phi, \chi) \sim \sqrt{\frac{-2\pi\hat{\varepsilon}}{\partial_{\hat{K}\hat{K}}\hat{\psi}\left(\hat{K}_s^{(j)}, \hat{Y}, \chi\right)}}\exp\left\{\frac{\hat{\psi}\left(\hat{K}_s^{(j)}, \hat{Y}, \phi, \chi\right)}{\hat{\varepsilon}}\right\}, \tag{3.3}$$

with

$$\hat{\psi}\left(\hat{K}_s^{(j)}, \hat{Y}, \phi, \chi\right) = -\hat{Y}\sqrt{\hat{K}_s^{(j)}} + \mathrm{i}\mathrm{e}^{\mathrm{i}\phi}\hat{K}_s^{(j)} - \mathrm{e}^{\mathrm{i}\chi}\left(\hat{K}_s^{(j)}\right)^2, \tag{3.4a}$$

$$\partial_{\hat{K}\hat{K}}\hat{\psi}\left(\hat{K}_s^{(j)}, \hat{Y}, \chi\right) = \frac{\hat{Y}}{4\hat{K}_s^{(j)}\sqrt{\hat{K}_s^{(j)}}} - 2\mathrm{e}^{\mathrm{i}\chi}. \tag{3.4b}$$

The main difficulty is to determine which saddle point contributes to the integral as the parameters $\hat{Y}$, ϕ and χ vary. *A priori* this requires the detailed analysis of the constant phase contours in the complex $\hat{K}$-plane to determine whether the integration contour can be deformed to pass through the saddle points along a steepest-descent contour. When there are two saddle-point contributions, one is much larger than the other unless we have $\mathrm{Re}(\hat{\psi}_s^{(1)}) = \mathrm{Re}(\hat{\psi}_s^{(2)})$, where $\hat{\psi}_s^{(j)}$ is the phase evaluated at $\hat{K}_s^{(j)}$ ($j = 1, 2$). For a given χ, this condition defines Stokes lines in the parameter space $(\hat{Y}, \phi)$. Along Stokes lines, both saddle-point contributions are of the same order, and as such a line is crossed, we expect the two saddle-point contributions to change dominance. Other important curves are defined by the anti-Stokes lines. These lines delimit regions in the parameter space where we may change from one to two saddle-point contributions. Accordingly, they are defined by $\mathrm{Im}(\hat{\psi}_s^{(1)}) = \mathrm{Im}(\hat{\psi}_s^{(2)})$. Thus, for a given χ, the problem of evaluating (3.1) reduces to determining the Stokes lines and the anti-Stokes lines in the parameter space $(\hat{Y}, \phi)$. (The Stokes line and anti-Stokes line terminology varies from one author to the other. Here we have followed the definition used by Bender & Orszag 1978).

Stokes lines and anti-Stokes lines satisfy particular properties near turning points $(\hat{Y}_c, \phi_c)$ where the saddle points merge. For instance, we know that three Stokes lines and three anti-Stokes lines issue from turning points with a $2\pi/3$ angle between two lines. The turning points can be obtained from

$$\partial_{\hat{K}}\hat{\psi} = \partial_{\hat{K}\hat{K}}\hat{\psi} = 0,$$

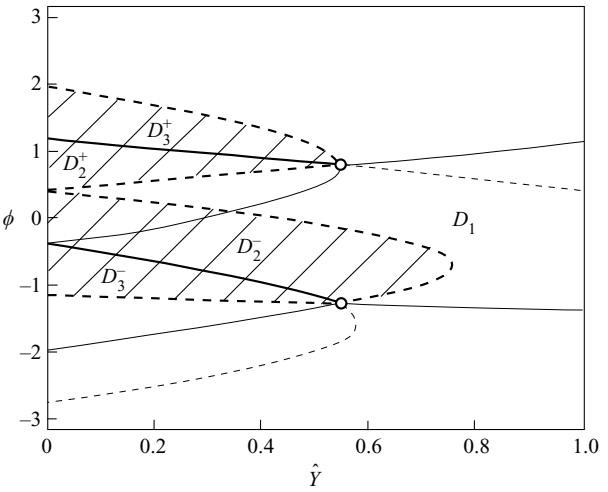

FIGURE 3. Stokes lines (solid lines) and anti-Stokes lines (dashed lines) in the parameter space $(\hat{Y}, \phi)$ for $\chi = \pi/4$. The circles are the turning points (or caustics) $T_c^{\pm}$. The thick lines delimit the different characteristic regions $D_j^{\pm}$.

which gives

$$\hat{K}_s^{(j)} = \frac{\mathrm{i}\mathrm{e}^{\mathrm{i}(\phi-\chi)}}{6} = \left(\frac{\hat{Y}\mathrm{e}^{-\mathrm{i}\chi}}{8}\right)^{2/3}. \tag{3.5}$$

We deduce two turning points $T_c^+ = (\hat{Y}_c, \phi_c^+) = ((2/3)^{3/2}, \chi/3 + \pi/6)$ and $T_c^- = (\hat{Y}_c, \phi_c^-) = ((2/3)^{3/2}, \chi/3 - \pi/2)$ with their associated double saddle points

$$\hat{K}_c^+ = \frac{\mathrm{e}^{(2\mathrm{i}/3)(\pi-\chi)}}{6}, \quad \hat{K}_c^- = \frac{\mathrm{e}^{-2\mathrm{i}\chi/3}}{6}. \tag{3.6}$$

It is easy to follow numerically in the parameter space the Stokes lines and anti-Stokes lines from each turning point. However, only two anti-Stokes lines and one Stokes line from each turning point are relevant in our problem, as in a large part of the parameter space, there is a single saddle-point contribution. Two saddle-point contributions are involved in the regions $D_j^{\pm}$ $(j = 2, 3)$ delimited by the anti-Stokes lines (figure 3). In these regions, the two contributions are of the same order on the Stokes lines. Each region delimited by a Stokes line or an anti-Stokes line corresponds to a region in which the integration contour in the integral (3.1) has to be deformed in a typical way (figure 4). Note that, in most cases, the position of the branch cut has to be modified such that the steepest-descent contour does not cross the branch cut. As $(\hat{Y}, \phi)$ rotates around the turning points, the saddle points tend to rotate around the associated double saddle point $\hat{K}_c^{\pm}$. Each performs a π rotation as a complete rotation of 2π is performed around the turning point. In order to unambiguously define the saddle points $\hat{K}_s^{(j)}$, it is therefore necessary to position two branch cuts issuing from each turning point in the $(\hat{Y}, \phi)$ space, as shown in figure 3 by the two Stokes lines $S^{\pm} = D_2^{\pm} \cap D_3^{\pm}$.

Suppose the saddle-point contribution in region D_1 is given by $I_s^{(1)}$. By shifting the original integration path from the real axis into the complex plane so that it follows a steepest-descent curve passing through one or two saddle points, the asymptotic

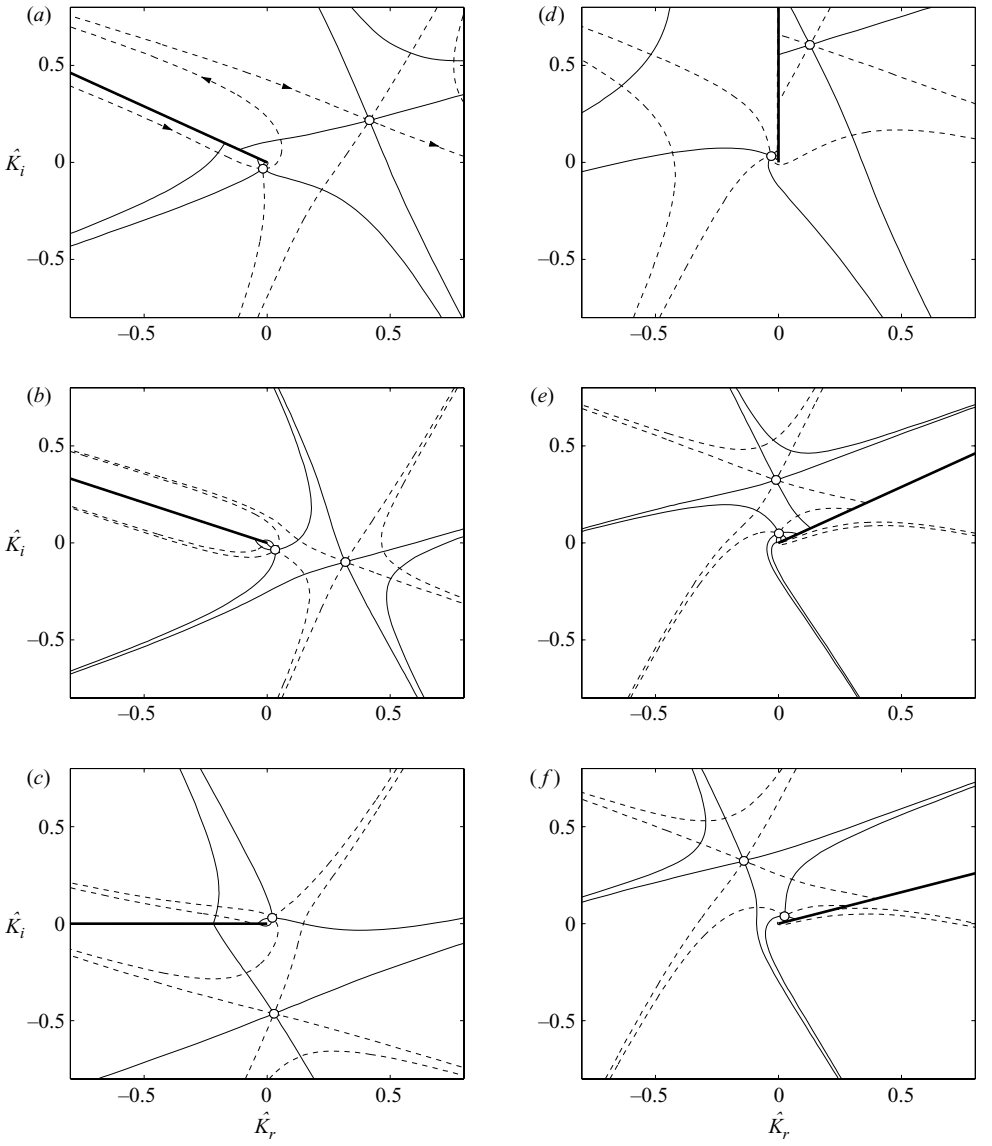

FIGURE 4. Typical constant-phase (steepest descent) contours of $\hat{\psi}$ (dashed lines) in the complex $\hat{K}$-plane. Solid lines are level curves on which the real part of $\hat{\psi}$ is constant. The branch cut is indicated by a thick solid line. Circles are saddle points. From (*a*) to (*c*), the region index varies in the region $\phi < 0$. The associated regions are respectively D_2^-, D_3^- and D_1, along the line $\hat{Y} = 0.4$. From (*d*) to (*f*), the region index varies in the region $\phi > 0$, from D_1 to D_3^+ along the line $\hat{Y} = 0.4$. The figures (*c*) and (*d*) correspond to the same region D_1, but with two different positions of the branch cut and for different parameters, respectively, $\phi = -2$ and $\phi = 1/2$.

behaviour of I is completely determined by

$$I \sim \begin{cases} I_s^{(1)} & (\hat{Y}, \phi) \in D_1, \\ I_s^{(1)} + I_s^{(2)} & (\hat{Y}, \phi) \in D_{2,3}^{\pm}, \end{cases} \tag{3.7}$$

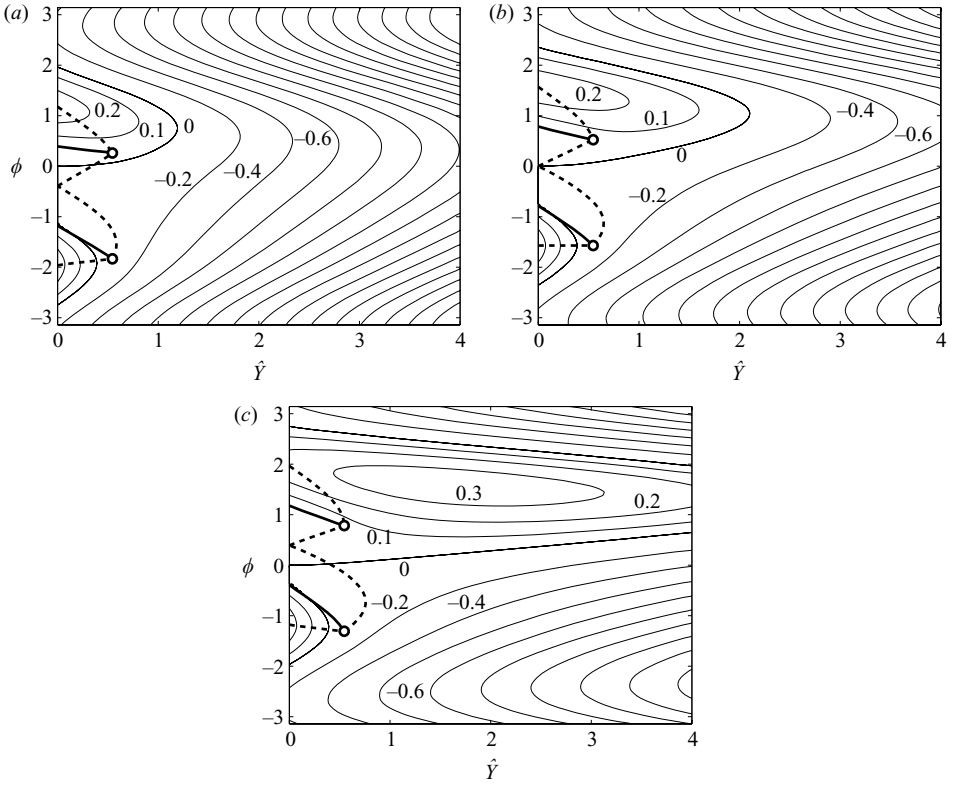

FIGURE 5. Level contours of $\mathrm{Re}(\hat{\psi}^{(1)})$ in the $(\hat{Y}, \phi)$-plane for (*a*) $\chi = -\pi/4$, (*b*) $\chi = 0$ and (*c*) $\chi = \pi/4$. The Stokes lines and anti-Stokes lines delimiting characteristic regions are, respectively, represented by solid and dashed lines. The turning points (or caustics) are plotted as circles.

where $I_s^{(1)}$ and $I_s^{(2)}$ are given by (3.3). The above approximation is also valid on the Stokes lines S^+ and S^-. With our definition for $\hat{K}_s^{(1)}$, the contribution from the other saddle point $\hat{K}_s^{(2)}$ remains exponentially small up to the Stokes lines on which both contributions are of the same order. In terms of asymptotic approximations (in the sense of Poincaré), (3.7) can be written

$$I \sim \begin{cases} I_s^{(1)} & (\hat{Y}, \phi) \notin S^{\pm}, \\ I_s^{(1)} + I_s^{(2)} & (\hat{Y}, \phi) \in S^{\pm}. \end{cases} \tag{3.8}$$

The form of the saddle-point contribution tells us that the modulus of I is governed almost everywhere by the levels of $\mathrm{Re}(\hat{\psi}^{(1)})$. In figure 5, these levels are plotted in the $(\hat{Y}, \phi)$-plane together with the Stokes and anti-Stokes lines for different values of χ. At the turning points $T_c^{\pm}$, both approximations for $I_s^{(1)}$ and $I_s^{(2)}$ diverge owing to the vanishing of $\partial_{\hat{K}\hat{K}}\hat{\psi}$. These points are so-called 'caustics' of the acoustic field. The existence of caustics has also been pointed out by Goldstein & Leib (2005) in a more general WKBJ framework, but they did not provide any solution valid near the caustics. Here, an adequate approximation for I near the caustics is obtained in the next section. Note also that when $\hat{Y}$ goes to zero, one of the two saddle points collapses with the branch point $\hat{K} = 0$. The contribution from the saddle point $\hat{K} = 0$

is, in that case, no longer given by an expression of the form (3.3), but by another expression that we shall derive in § 3.3.

3.2. *Approximation near the caustics*

The method for obtaining an approximation of the integral I near a caustic is classical and presented in several textbooks (see e.g. Kravtzov & Orlov 1990). The idea is to reduce the integral I in a suitable neighbourhood of $T_c^{\pm}$ to the caustic normal form which describes the singularity. Here the caustic is a fold singularity, that is the simplest catastrophe (Arnold 1978). This singularity is described by the Airy function

$$\mathrm{Ai}(x) = \frac{1}{2\pi}\int_{-\infty}^{+\infty} \exp\left\{\mathrm{i}\frac{u^3}{3} + \mathrm{i}ux\right\} \mathrm{d}u.$$

It is easy to see by expanding $\hat{\psi}$ in Taylor expansions with respect to $\hat{Y}_c$, $\phi_c^{\pm}$ and $\hat{K}_c^{\pm}$, that expression (3.1) for I can be written as

$$I \sim \frac{\hat{\varepsilon}^{1/3} \exp\left\{\dfrac{\hat{\psi}_c + \hat{\psi}_{\hat{Y}}\delta\hat{Y} + \hat{\psi}_{\phi}\delta\phi^{\pm}}{\hat{\varepsilon}}\right\}}{\left(-\dfrac{\mathrm{i}}{2}\hat{\psi}_{\hat{K}\hat{K}\hat{K}}\right)^{1/3}} \mathrm{Ai}\left\{\frac{\hat{\psi}_{\hat{Y}\hat{K}}\delta\hat{Y} + \hat{\psi}_{\phi\hat{K}}\delta\phi^{\pm}}{\left(-\dfrac{\mathrm{i}\hat{\varepsilon}^2}{2}\hat{\psi}_{\hat{K}\hat{K}\hat{K}}\right)^{1/3}}\right\}, \tag{3.9}$$

in the region defined by $\delta\hat{Y} = O(\hat{\varepsilon}^{2/3})$ and $\delta\phi^{\pm} = O(\hat{\varepsilon}^{2/3})$, where $\delta\hat{Y} = \hat{Y} - \hat{Y}_c$ and $\delta\phi^{\pm} = \phi - \phi_c^{\pm}$. In this expression, the derivatives are evaluated at the turning points. By applying (3.9) near the turning points T_c^+ and T_c^-, the integral I can finally be written, respectively,

$$I \sim Q \exp\left\{\frac{1 + 2\sqrt{6}\delta\hat{Y} - 2\mathrm{i}\delta\phi^+}{12\mathrm{e}^{\mathrm{i}(\chi-\pi)/3}\hat{\varepsilon}} + \frac{11\mathrm{i}\pi}{18}\right\} \mathrm{Ai}\left(\frac{\delta\hat{Y} - \mathrm{i}\sqrt{\frac{2}{3}}\delta\phi^+}{3^{1/6}\sqrt{2}\mathrm{e}^{\mathrm{i}(6\chi+\pi)/9}\hat{\varepsilon}^{2/3}}\right), \tag{3.10a}$$

$$I \sim Q \exp\left\{\frac{-1 - 2\sqrt{6}\delta\hat{Y} + 2\mathrm{i}\delta\phi^-}{12\mathrm{e}^{\mathrm{i}\chi/3}\hat{\varepsilon}} + \frac{9\mathrm{i}\pi}{18}\right\} \mathrm{Ai}\left(\frac{\delta\hat{Y} - \mathrm{i}\sqrt{\frac{2}{3}}\delta\phi^-}{3^{1/6}\sqrt{2}\mathrm{e}^{\mathrm{i}(2\chi+3\pi)/9}\hat{\varepsilon}^{2/3}}\right). \tag{3.10b}$$

with

$$Q = \frac{\hat{\varepsilon}^{1/3}\mathrm{e}^{-10\mathrm{i}\chi/18}}{9^{1/3}}. \tag{3.11}$$

3.3. *Approximation for small $\hat{Y}$*

When $\hat{Y}$ tends to zero, one of the two saddle points tends to the branch-point singularity $\hat{K} = 0$. Expansions for both saddle points as $\hat{Y} \to 0$ are easily obtained as

$$\hat{K}_s^{(0)} = -\frac{\mathrm{e}^{-2\mathrm{i}\phi}}{4}\left(\hat{Y}^2 + \mathrm{i}\mathrm{e}^{\mathrm{i}(\chi-3\phi)}\hat{Y}^4\right) + O(\hat{Y}^6), \tag{3.12a}$$

$$\hat{K}_s = \frac{\mathrm{i}}{2}\mathrm{e}^{\mathrm{i}(\phi-\chi)} - \frac{\hat{Y}}{2\sqrt{2}}\mathrm{e}^{\mathrm{i}(\phi+\chi)/2}\mathrm{e}^{-\mathrm{i}\pi/4} + O(\hat{Y}^2), \tag{3.12b}$$

where the saddle point which is close to the branch point $\hat{K} = 0$ as $\hat{Y}$ tends to zero is designated by $\hat{K}_s^{(0)}$. According to the general expression (3.3), the saddle-point

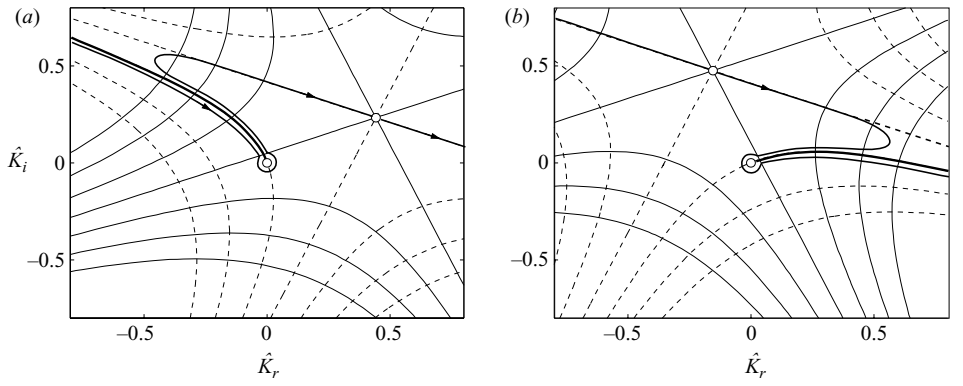

FIGURE 6. Typical contour plots when there is a branch-point contribution. The branch cut, indicated by a thick solid curve, has been deformed to be aligned along with a contour of constant imaginary part of $\hat{\psi}$. (*a*) $\hat{Y}=0$ and $\phi=-0.3$. (*b*) $\hat{Y}=0$ and $\phi=1.1$ (note that the branch cut has been moved to the other side of the saddle point).

contributions can be written, respectively, as

$$I_s^{(0)} \sim \hat{Y}\sqrt{\pi\hat{\varepsilon}}\,\mathrm{e}^{-3\mathrm{i}\phi/2}\exp\left\{\frac{\mathrm{i}\mathrm{e}^{-\mathrm{i}\phi}}{4\hat{\varepsilon}}\hat{Y}^2-\frac{\mathrm{e}^{\mathrm{i}(\chi-4\phi)}}{16\hat{\varepsilon}}\hat{Y}^4-\mathrm{i}\frac{\pi}{4}+O\left(\frac{\hat{Y}^6}{\hat{\varepsilon}}\right)\right\}, \tag{3.13a}$$

$$I_s \sim \sqrt{\pi\hat{\varepsilon}}\,\mathrm{e}^{-\mathrm{i}\chi/2}\exp\left\{-\frac{\mathrm{e}^{\mathrm{i}(2\phi-\chi)}}{4\hat{\varepsilon}}-\frac{\mathrm{e}^{\mathrm{i}\pi/4}\mathrm{e}^{\mathrm{i}(\phi-\chi)/2}}{2\hat{\varepsilon}}\hat{Y}+O\left(\frac{\hat{Y}^2}{\hat{\varepsilon}}\right)\right\}. \tag{3.13b}$$

Note that in order to determine the amplitude of $I_s^{(0)}$ as ϕ tends to zero, we have kept terms up to $\hat{Y}^4/\hat{\varepsilon}$ in (3.13*a*). Note also that the Stokes and anti-Stokes lines that delimit the regions in figure 3 may be computed from the phases in (3.13*a*) and (3.13*b*). We obtain $\phi_S^{\pm}=\chi/2\pm\pi/4$ for the Stokes lines, $\phi_{AS}=\chi/2$ and $\phi_{AS}^{\pm}=\chi/2\pm\pi/2$ for the anti-Stokes lines, which is in total agreement with figure 3. Indeed, the two anti-Stokes lines issued from the turning points merge at $\phi_{AS}=\chi/2$ for $\hat{Y}=0$.

The correspondence between $\hat{K}_s^{(1)}$, $\hat{K}_s^{(2)}$ and the saddle points defined by (3.12*a*) and (3.12*b*) can be established using (3.2). We find

$$\hat{K}_s^{(1)}=\begin{cases}\hat{K}_s^{(0)}, & \phi_S^-<\phi<\phi_S^+,\\ \hat{K}_s, & \phi<\phi_S^- \quad\text{or}\quad \phi>\phi_S^+,\end{cases} \tag{3.14}$$

and the complementary relation for $\hat{K}_s^{(2)}$. From (3.7), we deduce

$$I\sim\begin{cases}I_s, & \phi<\phi_{AS}^- \quad\text{or}\quad \phi>\phi_{AS}^+,\\ I_s^{(0)}+I_s, & \phi_{AS}^-<\phi<\phi_{AS}^+.\end{cases} \tag{3.15}$$

It is important to keep in mind that the steepest-descent method requires a large phase term $\hat{\psi}/\hat{\varepsilon}$. Here, this condition implies that $\hat{Y}$ must satisfy

$$\hat{Y}^2\gg\hat{\varepsilon}, \tag{3.16}$$

or equivalently, $y^2\gg N(\hat{X})\mu/\varepsilon$. When this condition is not satisfied, the saddle point $\hat{K}_s^{(0)}$ merges with the branch point $\hat{K}=0$ and approximation (3.15) is *a priori* no longer valid. The saddle-point contribution is transformed into a branch-point contribution. Such a contribution is present when the steepest-descent contour has to be deformed around the branch point (figure 6). The branch-point contribution comes from the

origin $\hat{K}=0$ in the vicinity in which the phase is dominated by the linear term $\mathrm{i}\mathrm{e}^{\mathrm{i}\phi}\hat{K}$. This contribution can be captured by performing the change of variable

$$-\eta = \mathrm{i}\mathrm{e}^{\mathrm{i}\phi}\hat{K}/\hat{\varepsilon}. \tag{3.17}$$

Substituting (3.17) into (2.22*b*) gives

$$\hat{\psi} = -\eta\hat{\varepsilon} + \mathrm{e}^{\mathrm{i}(\chi-2\phi)}(\eta\hat{\varepsilon})^2 - \hat{Y}\mathrm{e}^{-\mathrm{i}\phi/2-\mathrm{i}\pi/4}\sqrt{-\eta\hat{\varepsilon}}. \tag{3.18}$$

As soon as we have $\hat{Y}^2 \ll \hat{\varepsilon}$, the contribution coming from the neighbourhood of the branch point is obtained from

$$I_{cut} \sim -\mathrm{i}\mathrm{e}^{-\mathrm{i}\pi/4}\hat{Y}\sqrt{\hat{\varepsilon}}\mathrm{e}^{-3\mathrm{i}\phi/2}\int_{F_\eta}\sqrt{-\eta}\mathrm{e}^{-\eta}\,\mathrm{d}\eta, \tag{3.19}$$

with the Hankel's contour integral

$$\int_{F_\eta}\sqrt{-\eta}\mathrm{e}^{-\eta}\,\mathrm{d}\eta = \mathrm{i}\sqrt{\pi}, \tag{3.20}$$

where the path of integration starts at $+\infty$ on the real axis, circles the origin in a counterclockwise direction and returns to the starting point. Finally, we obtain

$$I_{cut} \sim \mathrm{e}^{-\mathrm{i}\pi/4}\hat{Y}\sqrt{\pi\hat{\varepsilon}}\mathrm{e}^{-3\mathrm{i}\phi/2}. \tag{3.21}$$

This expression corresponds to the leading-order expression of $I_s^{(0)}$ for $\hat{Y}^2/\hat{\varepsilon} \ll 1$. As the contribution for the other saddle point $\hat{K}_s$ is not modified for $\hat{Y}^2 \ll \hat{\varepsilon}$, this implies that the approximations (3.13*a*, *b*) are also valid when $\hat{Y}^2 \ll \hat{\varepsilon}$.

4. Acoustic near field

In the previous section, we have obtained approximations for the generic integral I that intervenes in the expression of the acoustic field. In the present section, these approximations are used to plot the level contours of the acoustic near field in the physical space (x, y).

Expressions for ϕ and $\hat{Y}$ in terms of x and y can be deduced from (2.15*a*, *b*), (2.19*a*, *b*) and (2.20). If we use the expression $\bar{\alpha}\mu = (1/M_c - 1)$ where M_c is the convective Mach number, we obtain

$$\phi = \arg\left(x - x_m + \mathrm{i}\mathrm{e}^{\mathrm{i}\chi}\frac{1-1/M_c}{\bar{\varepsilon}}\right), \tag{4.1a}$$

$$\hat{Y} = \frac{y}{\sqrt{\bar{\varepsilon}}}\left|x - x_m + \mathrm{i}\mathrm{e}^{\mathrm{i}\chi}\frac{1-1/M_c}{\bar{\varepsilon}}\right|^{-3/2}. \tag{4.1b}$$

Similarly, we can express x and y in terms of ϕ and $\hat{Y}$. We obtain

$$x = x_m + \frac{1-1/M_c}{\bar{\varepsilon}}\left[\sin(\chi) + \frac{\cos(\chi)}{\tan(\phi)}\right], \tag{4.2a}$$

$$y = \frac{|1-1/M_c|^{3/2}}{\bar{\varepsilon}}\left|\frac{\cos\chi}{\sin\phi}\right|^{3/2}\hat{Y}. \tag{4.2b}$$

Note that the parameter $\bar{\varepsilon}$ is also related to physical quantities: it is given by $\bar{\varepsilon} = |\alpha_c'/\alpha_c^2|$.

In the limit of vanishing $\bar{\varepsilon}$, we have seen that, almost everywhere, the integral I can be estimated by a single saddle-point contribution $I_s^{(1)}$ whose amplitude is dominated

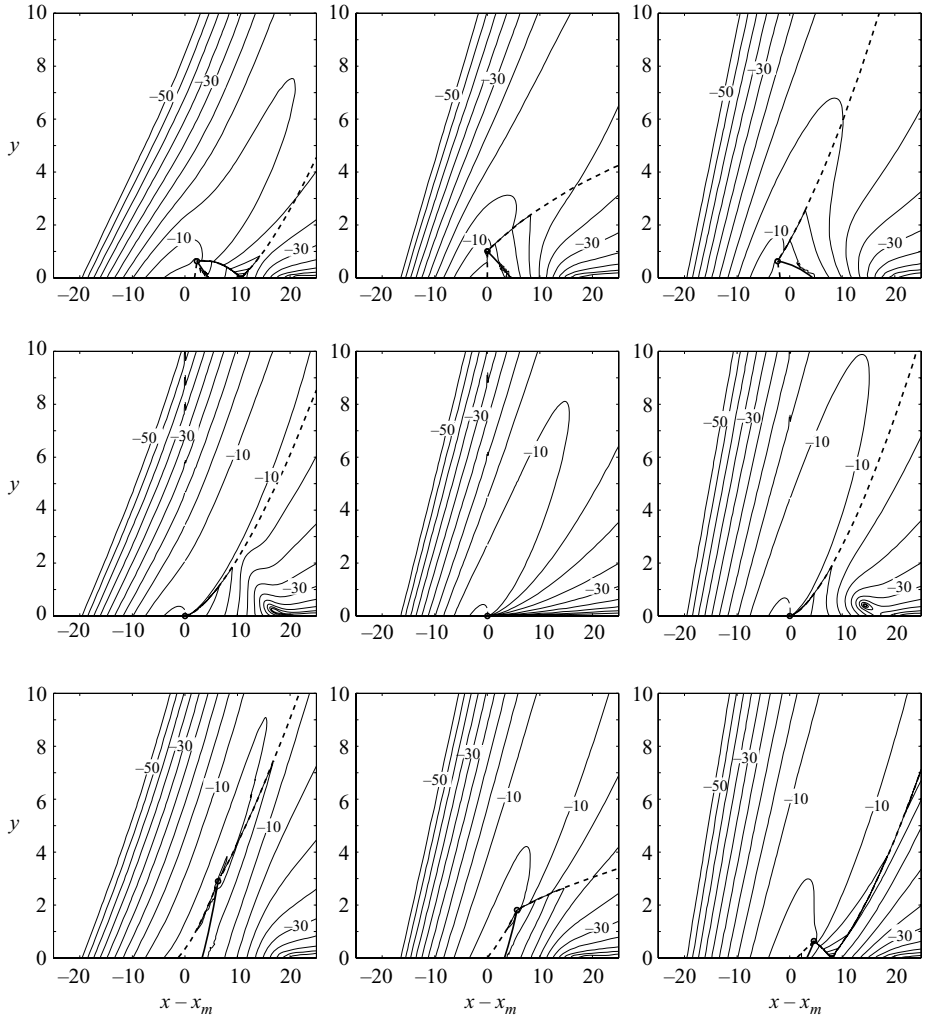

FIGURE 7. Sound pressure levels in the physical (x, y) space. The Mach number is 0.85 in the top line, 1 in the middle line and 1.15 in the bottom line. The parameter χ is $-\pi/4$, 0 and $\pi/4$ in the left-hand row, middle row and right-hand row, respectively. The caustic (circle), the Stokes lines (thick solid curves) and the anti-Stokes lines (thick dashed lines) are also indicated. The parameter $\bar{\varepsilon}$ is here $\bar{\varepsilon} = 0.04$.

by the levels of $\mathrm{Re}(\hat{\psi}_s^{(1)})$ which have been displayed in figure 5. In this limit, the main behaviour of p can be deduced from these figures using (2.21) and the mapping (4.1). For small but finite value of $\bar{\varepsilon}$, both the amplitude factor and the second subdominant contribution create amplitude corrections which can become non-negligible. In figure 7, the complete approximation obtained from (3.7) is plotted for a given value $\bar{\varepsilon} = 0.04$. The sound pressure levels defined by

$$Sp = 10 \log_{10} \langle p^2 \rangle$$

are given for three different values of χ and three different Mach numbers. Note that we have normalized the pressure such that $Sp = 0$ at the maximum of the instability wave. These pressure levels therefore measure the transmission loss of the instability

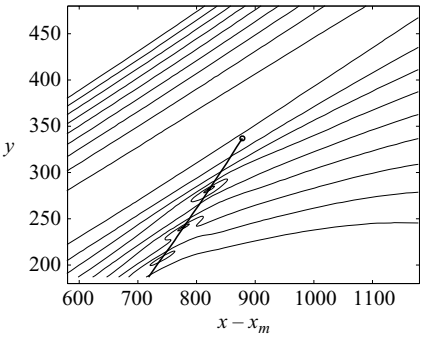

FIGURE 8. Sound pressure levels near the caustic (circle). The solid line corresponds to the Stokes line on which local minima of pressure are present. Here, $M_c = 1.1$, $\bar{\varepsilon} = 0.0002$ and $\chi = -\pi/4$.

wave in the plane. The caustic point, the Stokes and anti-Stokes lines are also indicated in figure 7. The anti-Stokes lines delimit the region where the acoustic field is approximated by the sum of two contributions. Near the anti-Stokes line, the subdominant contribution is exponentially small in the limit of small $\bar{\varepsilon}$. Here, the finite value of $\bar{\varepsilon}$ induces a weak discontinuous behaviour across the anti-Stokes line.

Characteristic features can be noted from these plots. Whatever χ and the convective Mach number, the acoustic field is a maximum along a direction whose angle varies between $\pi/8$ and $\pi/4$. The peak angle increases with χ and the convective Mach number. Note also that the maximum is always located in a region where the pressure approximation has a single saddle-point contribution. The directivity pattern of the pressure field is therefore not due to the presence of several contributions. As expected, we can also see that the acoustic field is weak for subsonic Mach numbers, but strong for supersonic Mach numbers.

The caustic, indicated by a circle in figure 7, corresponds to a singularity of approximation (3.7). This point is given in physical variables by

$$x_c = x_m + \frac{2(1 - 1/M_c)}{\bar{\varepsilon}} \cos(\chi/3 + \pi/6), \tag{4.3a}$$

$$y_c = \frac{|1 - 1/M_c|^{3/2}}{\bar{\varepsilon}} \left| \frac{2\cos\chi}{3\sin(\chi/3 + \pi/6)} \right|^{3/2}. \tag{4.3b}$$

Near such a point the local approximation (3.10*a*) or (3.10*b*) has to be used. Figure 8 shows the sound pressure level near the caustic obtained with this approximation for $\chi = -\pi/4$ and $M_c = 1.1$. A smaller value of $\bar{\varepsilon}$ than in figure 7 has been used in order to see the peculiar structure of the field near the caustic. Note in particular that the pressure field possesses a series of minima corresponding to the zeros of the Airy function. Near these minima, higher order terms have to be considered to derive an adequate approximation of the pressure field. These minima are located on the Stokes line. They are the signature of the destructive interactions of the two wave-like contributions $I_s^{(1)}$ and $I_s^{(2)}$.

5. Branch point contribution in the shear flow region

Close to the shear-flow region, $\hat{Y}$ becomes small and expressions (3.15) for I must be used to obtain an approximation for the pressure field. We have seen in § 3.3

that for small $\hat{Y}$, I possesses two possible contributions I_s and $I_s^{(0)}$ associated with a saddle point and a branch point, respectively. The pressure field p_s associated with the saddle-point contribution reduces, for $1 \ll y \ll 1/\sqrt{\varepsilon}$, to

$$p_s \sim p_{im}^{(\infty)}(x;\varepsilon)\exp\{-\sqrt{2[\alpha(X)-1]}y\}. \tag{5.1}$$

It exactly matches the instability wave approximation (2.2) for large y, when the wave is close to transonic. The pressure field p_{cut} associated with the branch-point contribution $I_s^{(0)}$ can be simplified to:

$$p_s^{(0)} \sim \hat{p}_{im}^{(\infty)} \frac{y\sqrt{2\pi}\mathrm{e}^{\mathrm{i}x-\mathrm{i}\pi/4}}{\left(x - x_m + \mathrm{i}\mathrm{e}^{\mathrm{i}\chi}\dfrac{1-1/M_c}{\bar{\varepsilon}}\right)^{3/2}}, \tag{5.2}$$

using (2.12). This expression is in agreement with (2.8) for small inclination angles.

As shown in § 3.3, the instability wave contribution is present everywhere. The branch-cut contribution appears when the anti-Stokes angle $\phi_{AS}^{\pm} = \chi/2 \pm \pi/2$ is crossed, and becomes dominant when we cross the Stokes angle $\phi_S^{\pm} = \chi/2 \pm \pi/4$. In terms of real variables, this means that the branch-cut contribution appears in the pressure-field approximation downstream of the location

$$x_{AS} = x_m + \frac{1-1/M_c}{\bar{\varepsilon}}\tan(\chi/2), \tag{5.3}$$

and becomes dominant downstream of

$$x_S = x_m + \frac{|1-1/M_c|}{\bar{\varepsilon}}. \tag{5.4}$$

These two characteristic locations can also be obtained easily from geometrical arguments. Indeed, the phase given by (2.18*b*), from which we deduce the different contributions, can be simplified for small $\bar{Y}$ as

$$\mu^2\psi = -\frac{\mathrm{e}^{\mathrm{i}\chi}}{2}\left[\bar{K} - \left(\frac{1}{M_c}-1\right) - \bar{\varepsilon}\mathrm{i}\mathrm{e}^{-\mathrm{i}\chi}(x-x_m)\right]^2. \tag{5.5}$$

Thus, the instability-wave contribution comes from the saddle point

$$\bar{K}_s = 1/M_c - 1 + \bar{\varepsilon}\mathrm{i}\mathrm{e}^{-\mathrm{i}\chi}(x-x_m) \sim \alpha(X) - 1. \tag{5.6}$$

In figure 9, this point and the characteristic curves $\mathrm{Re}(\psi)=0$ and $\mathrm{Im}(\psi)=0$ are plotted in the complex $\bar{K}$-plane. The branch cut issued from $\bar{K}=0$ is also indicated. The existence of the branch-cut contribution depends on the position of branch point $\bar{K}=0$ with respect to the characteristic curves. If the branch point is in the sector A limited by the steepest descent path (on which $\mathrm{Im}(\psi)=0$), the branch-point contribution is present (see figure 6). Moreover, this contribution is larger than the saddle-point contribution if it possesses a larger $\mathrm{Re}(\psi)$, that is, if the branch point is in the sector B limited by $\mathrm{Re}(\psi)=0$ curves. Both (5.3) and (5.4) can be obtained by taking $\bar{K}=0$ to be on the boundaries of the sectors A and B, respectively.

A third sector, C, has also been indicated in figure 9. When the branch point is in this sector, the branch cut has to be displaced to the other side of the saddle point for the steepest descent path to go through this point (as illustrated in figure 6*b*). This means that $\sqrt{\bar{K}_s}$ is on the second Riemann sheet on which $\mathrm{Re}(\sqrt{\bar{K}_s}) < 0$. In view of (5.6) and (5.1), this implies that the instability-wave contribution has an exponentially

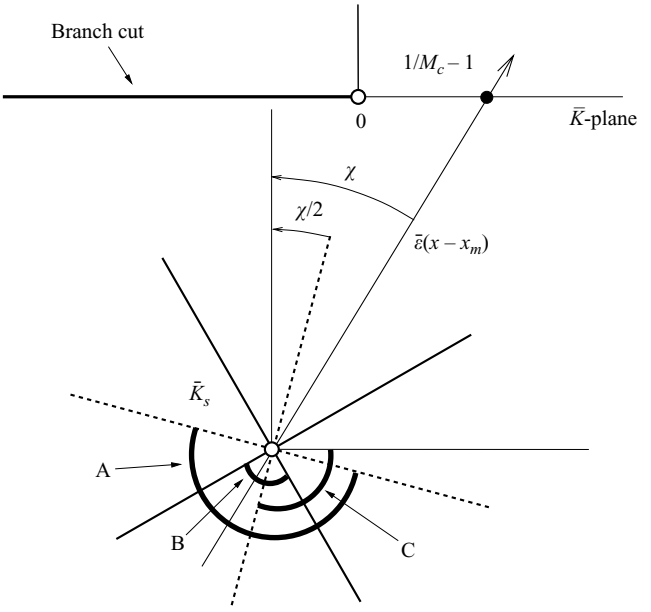

FIGURE 9. Phase contours for small $\hat{Y}$. Location in the complex $\bar{K}$-plane of the saddle point $\bar{K}_s$, the characteristic curves $\mathrm{Re}(\psi) = 0$ (solid lines) and $\mathrm{Im}(\psi) = 0$ (dashed lines) with respect to the branch cut (thick solid line). The pressure field approximation possesses specific features when the branch point $\bar{K} = 0$ is in the sectors A, B and C (see text).

growing behaviour with respect to y in this sector. This peculiar transverse behaviour of the instability wave occurs in the following physical regions:
For $M_c > 1$:

$$0 < x - x_m < \frac{1 - 1/M_c}{\bar{\varepsilon}\tan(\chi/2)} \quad \text{if} \quad \chi > 0, \tag{5.7a}$$

$$0 < x - x_m \quad \text{if} \quad \chi < 0. \tag{5.7b}$$

For $M_c < 1$:

$$\frac{1 - 1/M_c}{\bar{\varepsilon}\tan(\chi/2)} < x - x_m \quad \text{if} \quad \chi < 0. \tag{5.8a}$$

It is worth mentioning that the exponentially growing behaviour of the instability wave is neither directly related to the existence of a branch point contribution nor to the supersonic character of the instability wave. It can occur in both subsonic and supersonic cases and also in configurations in which there is no branch-point contribution. However, it always occurs downstream of the maximum amplitude of the instability wave, that is, in regions where the wave is spatially damped. However, again, being downstream of X_m is not a sufficient condition for either supersonic nor subsonic waves.

The boundaries of the different regions associated with the sectors A, B and C where the pressure-field approximation changes in nature can be expressed in terms of a single rescaled variable

$$\xi = \bar{\varepsilon}\frac{x - x_m}{|1 - 1/M_c|}. \tag{5.9}$$

These boundaries are plotted in figure 10.

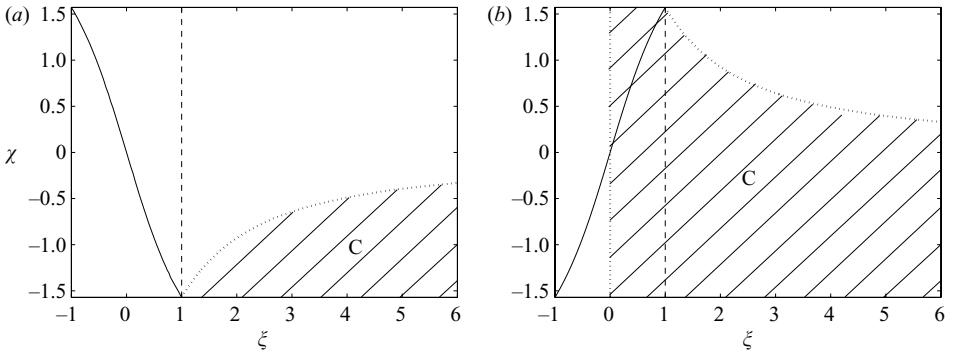

FIGURE 10. Curves in the (ξ, χ)-plane where the pressure near field (for small $\hat{Y}$) changes in nature. (*a*) $M_c < 1$; (*b*) $M_c > 1$. The branch-point contribution is present on the right-hand side of the solid line (sector A), and dominant on the right-hand side of the dashed line (sector B). The instability wave exhibits an exponentially growing transverse behaviour (sector C) on the right-hand side of the dotted line, except for $M_c > 1$ and $\xi > 0$ for which such a behaviour occurs in between the two dotted lines.

6. Discussion

In this article, we have analysed the acoustic near field generated by a close-to-transonic instability wave. We have shown that the conversion of the instability wave into an acoustic field is governed by the structure of the perturbation in the near-field region close to the location X_m where the instability wave reaches its maximum. By a local analysis near X_m, we have been able to determine the generic structure of the acoustic near field. Using a steepest descent method, approximations for the acoustic near field have been derived. We have shown that the acoustic field is either composed of a single saddle-point contribution or of two saddle-point contributions. The region where two contributions are present has been determined. A caustic where the two saddle points merge has also been identified. A specific approximation for the acoustic field has been obtained near such a point.

The acoustic near field close to the shear-flow region has also been studied. We have shown that two contributions are present downstream of a location which has been calculated. One of these contributions reduces to the instability wave whereas the other one, associated with a branch-point singularity, is an algebraic field which is in agreement with the far-field expression of the acoustic field. The algebraic contribution becomes dominant over the instability wave downstream a specific location. We have also demonstrated that the instability wave should have an exponentially growing transverse behaviour in certain regions downstream of X_m to match the acoustic field. This peculiar behaviour of the instability wave had been noticed by Tam & Burton (1984*a*) for supersonic convective Mach numbers. Here, we have provided an explanation and identified the parameters governing this phenomenon for both supersonic and subsonic convective Mach numbers.

We would be interested to compare our predictions for the acoustic near field with numerical and experimental data. Unfortunately, we have not found any data of the acoustic near field generated by a transonic wave packet in a two-dimensional flow. Tam & Morris (1980) provided some predictions for the noise directivity in the far field using the local stability properties of a spatially developing wave packet in a two-dimensional shear layer. Their stability results can be used to calculate the near field in our framework. For the strongest Mach number they considered

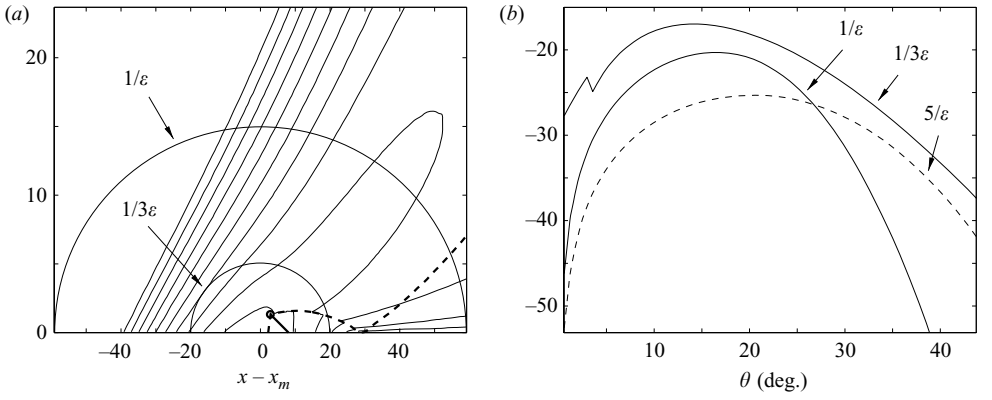

FIGURE 11. (*a*) Sound pressure levels in the physical (x, y)-space and (*b*) acoustic near-field directivity for $M_c = 0.88$, $\chi = -0.54$ and $\bar{\varepsilon} = 0.017$. The dashed line corresponds to the acoustic far field.

($M = 1.75$), the convective Mach number of their temporally forced instability wave is approximatively $M_c \simeq 0.88$ and we can estimate $\chi \simeq -0.54$ and $\bar{\varepsilon} \simeq 0.017$ using figures 3 and 4 of their paper. Figure 11(*a*) shows the sound pressure levels for the instability wave packet corresponding to these parameters. The near-field directivity patterns are shown in figure 11(*b*) for several radial distances from x_m and compared to the acoustic far field given by (2.8) with (2.12). Note first that the far-field directivity peaks at 20° and possesses a similar form to the directivity pattern obtained by Tam & Morris (1980) (compare with figure 14 of Tam & Morris 1980 for angles between 0 and 40°). This means that our Gaussian approximation for the wave packet is sufficient to capture the main feature of the directivity pattern in the far field in that case. Secondly, it is worth pointing out that the directivity pattern varies in the near field. In particular, the peak angle decreases as we become closer to the instability wave maximum. Note also that the width of the peak does not have a monotonous behaviour: the directivity pattern has its more pronounced peak at a distance approximatively equal to the integral scale $1/\bar{\varepsilon}$. Tam & Morris (1980) also noticed that the radiation patterns are similar for all frequencies. Here, this property is obtained in a straightforward manner by simply noticing that none of the parameters M_c, χ and $\bar{\varepsilon}$ depends on the frequency.

As already mentioned in § 1, there are many works on both subsonic and supersonic jets. For instance, Mitchell *et al.* (1997) computed the acoustic near field of a supersonic wave packet in an axisymmetric $M = 2$ jet. They obtained, by direct numerical simulation, sound pressure patterns which resemble our results (see their figure 4). Yet, our results cannot be applied directly to their case. The behaviour of the perturbations in the near field of a jet involves special functions which have not been taken into account in our analysis. In particular, Bessel functions should be present in the integral expression (2.6) of the acoustic near field. These functions modify the near-field characteristics, but they do not affect the directivity pattern in the far field. Therefore, it is not surprising that some characteristics of the acoustic far field associated with perturbations in jets can still be captured by our analysis.

Although the general agreement of the directivity of the Mach wave radiation and its peak Strouhal number are indirect evidence supporting the linear theory, the recent numerical simulation of Mohseni *et al.* (2002) indicates that nonlinear effects may be of importance in sound fields of supersonic jets. Nonlinear effects are expected to

affect the characteristics of instability wave packets, but if the acoustic propagation remains linear, our analysis can *a priori* still be used. It would be interesting to analyse the modifications of the sound field associated with these effects in our framework.

REFERENCES

Arnold, V. I. 1978 *The Mathematical Methods of Classical Mechanics*. Springer.

Avital, E. J. & Sandham, N. D. 1997 A note on the structure of the acoustic field emitted by a wave packet. *J. Sound Vib.* **204**, 533–539.

Bender, C. M. & Orszag, S. A. 1978 *Advanced Mathematical Methods for Scientists and Engineers*. McGraw-Hill.

Colonius, T., Lele, S. K. & Moin, P. 1997 Sound generation in a mixing layer. *J. Fluid Mech.* **330**, 375–409.

Cooper, A. J. & Crighton, D. G. 2000 Global modes and superdirective acoustic radiation in low-speed axisymmetric jets. *Eur. J. Mech.* B/*Fluids* **19**, 559–574.

Crighton, D. G. 1975 Basic principles of aerodynamic noise generation. *Prog. Aerospace Sci.* **16**, 31–96.

Crighton, D. G. & Huerre, P. 1990 Shear-layer pressure fluctuations and superdirective acoustic sources. *J. Fluid Mech.* **220**, 355–368.

Erdélyi, A. 1956 *Asymptotic Expansions*. Dover.

Freund, J. F. 2001 Noise sources in a low-Reynolds-number turbulent jet at Mach 0.9. *J. Fluid Mech.* **438**, 277–305.

Goldstein, M. E. 1984 Aeroacoustics of turbulent jet flows. *Annu. Rev. Fluid Mech.* **16**, 263–295.

Goldstein, M. E. & Leib, S. J. 2005 The role of instability waves in predicting jet noise. *J. Fluid Mech.* **525**, 37–72.

Kravtzov, Y. A. & Orlov, Y. I. 1990 *Geometrical Optics of Inhomogeneous Media*, Springer series on wave phenomena, vol. 6. Springer.

Laufer, J. & Yen, T. C. 1983 Noise generation by a low-Mach-number jet. *J. Fluid Mech.* **134**, 1–31.

Lighthill, M. J. 1952 On sound generated aerodynamically. i: General theory. *Proc. Roy. Soc. Lond.* A **211**, 564–587.

McLaughlin, D. K., Morrison, G. L. & Troutt, T. R. 1975 Experiments on the instability waves in a supersonic jet and their acoustic radiation. *J. Fluid Mech.* **69**, 73–95.

McLaughlin, D. K., Morrison, G. L. & Troutt, T. R. 1977 Reynolds number dependence in supersonic jet noise. *AIAA J.* **15**, 526–532.

Malik, M. R. & Chang, C.-L. 2000 Nonparallel and nonlinear stability of supersonic jet flow. *Comput. Fluids* **29**, 327–365.

Millet, C. & Casalis, G. 2004 Exponential-algebraic transition in the near-field of low supersonic jets. *Eur. J. Mech.* B/*Fluids* **23**, 367–379.

Mitchell, B. E., Lele, S. K. & Moin, P. 1997 Direct computation of Mach wave radiation in an axisymmetric supersonic jet. *AIAA J.* **35**, 1574–1579.

Mohseni, K., Colonius, T. & Freund, J. B. 2002 An evaluation of linear instability waves as sources of sound in a supersonic turbulent jet. *Phys. Fluids* **14**, 3593–3600.

Morris, P. J. & Tam, C. K. W. 1977 Near and far field noise from large-scale instabilities of axisymmetric jets. *AIAA Paper* 77-1351.

Morris, P. J., Long, L. N., Bangalore, A. & Wang, Q. 1997 A parallel three-dimensional computational aeroacoustics method using nonlinear disturbance equations. *J. Comput. Phys.* **133**, 56–74.

Morrison, G. L. & McLaughlin, D. K. 1980 Instability process in low Reynolds number supersonic jets. *AIAA J.* **18**, 793–800.

Stromberg, J. L., McLaughlin, D. K. & Troutt, T. R. 1980 Flow field and acoustic properties of a Mach number 0.9 jet at low Reynolds number. *J. Sound Vib.* **72**, 159–176.

Tam, C. K. W. 1995 Supersonic jet noise. *Annu. Rev. Fluid Mech.* **27**, 17–43.

Tam, C. K. W. & Burton, D. E. 1984*a* Sound generated by instability waves of supersonic flows. Part 1. Two dimensional mixing layers. *J. Fluid Mech.* **138**, 249–271.

Tam, C. K. W. & Burton, D. E. 1984*b* Sound generated by instability waves of supersonic flows. Part 2. Axisymmetric jets. *J. Fluid Mech.* **138**, 273–295.

Tam, C. K. W. & Morris, P. J. 1980 The radiation of sound by the instability waves of a compressible plane turbulent shear layer. *J. Fluid Mech.* **98**, 349–381.

Tam, C. K. W. & Chen, P. & Seiner, J. M. 1992 Relationship between instability waves and noise of high-speed jets. *AIAA J.* **30**, 1747–1752.

Troutt, T. R. & McLaughlin, D. K. 1982 Experiments on the flow and acoustic properties of a moderate Reynolds number supersonic jet. *J. Fluid Mech.* **116**, 123–156.

Yu, J. C. & Dosanjh, D. S. 1971 Noise field of coaxial interacting supersonic jet flow. *AIAA Paper* 71-152.